Sensors & Actuators: B. Chemical 433 (2025) 137565

Contents lists available at ScienceDirect

Sensors and Actuators: B. Chemical

journal homepage: www.elsevier.com/locate/snb

Edge-enriched SnS_2 nanosheets on graphene for chemiresistive room temperature NH_3 sensors

Lizhai Zhang [a,b,c,e,*], Jiayuan Xu [d], Xinyu Lei [a], Henghui Sun [a], Taotao Ai [a,*], Fei Ma [b,e], Paul K. Chu [c,**]

[a] School of Materials Science and Engineering, Shaanxi University of Technology, Hanzhong, Shaanxi 723001, China
[b] State Key Laboratory for Mechanical Behavior of Materials, Xi'an Jiaotong University, Xi'an, Shaanxi 710049, China
[c] Department of Physics, Department of Materials Science and Engineering, and Department of Biomedical Engineering, City University of Hong Kong, Kowloon, Hong Kong
[d] Natural Active Industrialization Engineering Technology Research Centre of Shaanxi Province, Shaanxi University of Technology, Hanzhong, Shaanxi 723001, China
[e] College of Physics and Information Technology, Shaanxi Normal University, Xi'an, Shaanxi 710062, China

ARTICLE INFO

Keywords:
Heterojunction
SnS_2/graphene composite
NH_3 sensing
First-principles calculation

ABSTRACT

Transition metal dichalcogenides (TMDs) with a larger surface area, abundant surface defect, and controlled electrical performance are promising in field of gas sensor. While, their drawbacks are low sensitivity, sluggish recovery kinetics, and poor selectivity. Herein, graphene is functionalized with SnS_2 nanosheets by a hydrothermal process. Compared to pure SnS_2 and graphene, the room-temperature response to 500 ppm NH_3 is about 91.32 %, which is increased by 1700 % and 63.63 %, respectively. With increase of temperature and humidity, the baseline resistance and NH_3-sensing response decreases strongly. The effect of temperature and humidity on resistance change of composites is high and the desired NH_3-sensing response of composites may not yet be reached due to its high sensitivity towards humidity and temperature fluctuations. Additionally, the room-temperature response to 100 ppm NO_2 is only about 17.83 %, which is much smaller than that of NH_3 (62.36 %) and the resistance couldn't recovery to initial value, behaving the poor recovery performance for NO_2. The Density-functional theory calculations reveal that the stronger NH_3 adsorption ability of SnS_2, higher carrier mobility of graphene, and more effective charge transfer at p-n heterointerface contribute to the enhancement.

1. Introduction

The large amount of ammonia (NH_3) released into the atmosphere during the production of agricultural fertilizers, medicines, textiles, and petrochemicals causes environmental and health hazards [1–4]. For example, long-term exposure to 50 ppm NH_3 causes eye irritation and skin burning, leading to discomfort and potential bacterial infection, and long-term exposure to 300 ppm NH_3 can damage human organs, causing pulmonary edema and bronchitis [1–4]. In medical diagnosis, an NH_3 concentration larger than 10 ppb in the breath of patients can be a sign of kidney failure [5], and therefore, accurate real-time detection of NH_3 is important clinically.

The SnS_2 with larger surface area, layered structure, and high carrier mobility, has large potential in NH_3 detection applications [6–10]. For example, *Qin et al.* have prepared two-dimensional SnS_2 with 1–3 layers by chemical exfoliation capable of detecting 20 ppm NH_3 representing a 32-fold enhancement compared to bulk SnS_2 [6]. *Xiong et al.* have synthesized thin SnS_2 nanosheets by a solvothermal method. Besides showing a response of 86.48 % to 100 ppm NH_3 at 200 ℃, a low detection limit (0.5 ppm) and high selectivity to NH_3 are observed [8]. *Zhang et al.* have prepared SnS_2 nanosheets by the solvothermal process in combination with argon plasma treatment showing excellent NH_3 sensing response at 100 ℃ [9]. However, these SnS_2 gas sensors still need a high working temperature while the sensitivity and sensing kinetics must be improved [10]. Hence, room-temperature SnS_2 gas sensors with high sensing response, high selectivity, and short recovery time are in high demand.

In order to enhance room-temperature NH_3 sensing properties of

* Corresponding authors at: School of Materials Science and Engineering, Shaanxi University of Technology, Hanzhong, Shaanxi 723001, China.
** Corresponding author at: Department of Physics, Department of Materials Science and Engineering, and Department of Biomedical Engineering, City University of Hong Kong, Tat Chee Avenue, Kowloon, Hong Kong.
E-mail addresses: zhanglizhai0512@snut.edu.cn (L. Zhang), aitaotao0116@126.com (T. Ai), paul.chu@cityu.edu.hk (P.K. Chu).

https://doi.org/10.1016/j.snb.2025.137565
Received 27 September 2024; Received in revised form 2 March 2025; Accepted 3 March 2025
Available online 4 March 2025

SnS_2, fabrication of SnS_2 based composites have been proposed [11–15]. *He et al.* have reported the room-temperature NH_3 sensing response of SnS_2 by combining with $Ti_3C_2T_x$. Without $Ti_3C_2T_x$, the SnS_2 behaves no response to10 ppm NH_3 at room temperature (RT), but the response of $SnS_2/Ti_3C_2T_x$ compounds is enhanced by 42.9 % at RT. And the NH_3 detection limit is reduced to 10 ppb [11]. *Bai et al.* have prepared composites of SnS_2 and SnO_2 hydrothermally showing high response to NH_3 at RT while offering the high selectivity, reliable long-term stability, as well as fast response and recovery rate [12]. Compared to MXene and metal oxides, graphene has larger surface area, higher conductivity, and carrier mobility [16–18]. Therefore, it is proposed that if SnS_2 is combined with graphene, the room-temperature NH_3 sensing response maybe improved.

Herein, the compounds of SnS_2 and graphene are prepared by a hydrothermal method. The graphene serves as the substrate for Sn^{4+} and S^{2-} ions adsorption, reaction, nucleation, and then growth of SnS_2 hexagonal nanosheets. During NH_3-sensing response, the graphene mainly serves as the underlying layer, providing the efficient channels for electron transport at RT and the SnS_2 mainly provides the active sites for NH_3 adsorption. The response results reveal that the composites behave the excellent response of 91.32 % for 500 ppm NH_3 at RT, which is approximately 1.57 and 18 times better than that of the pristine SnS_2 and graphene, respectively, along with the short response and recovery times, long-term stability, and low detection limit. The sensing mechanism and synergistic effects of p-n heterojunction between SnS_2 and graphene are investigated and discussed experimentally and theoretically.

2. Experimental details

2.1. Preparation of SnS_2 and graphene composites

As displayed in Fig. 1, the modified Hummers' method was used to prepare graphene [18]. In the preparation of SnS_2/graphene composites, the graphene powder was dissolved in 0.03 L of distilled water and sonicated for 1.5 h. $SnCl_4{\cdot}5\ H_2O$ (250 mg) and CH_4N_2S (350 mg) were added into solution and stirred for 120 min. The solution was transferred into a 50 mL autoclave and heated at 200 ℃ for 24 h. The prepared samples were washed with distilled water and ethanol three times and vacuum-dried at 60 ℃ for 720 min. To study the role of graphene on the sensing response, 0.2 *wt*% (0.5 mg), 0.4 *wt*% (1 mg), 2.5 *wt*% (5 mg), and 4 *wt*% (10 mg) graphene (Related to amount of $SnCl_4{\cdot}5\ H_2O$) were tested, and sampled as SnS_2/G-a, SnS_2/G-b, SnS_2/G-c and SnS_2/G-d, respectively. The pure SnS_2 was prepared by the same method without graphene.

2.2. Materials characterization

The crystal structure of SnS_2/graphene composites was measured by x-ray diffraction with Cu $K\alpha_1$ radiation (Bruker D8 Advance, $\lambda = 1.5406$ Å) in the 2θ range from 5° to 90°. The Raman spectra of SnS_2, graphene and composites were acquired by using the LabRAM HR Evolution with 532 nm laser excitation. To examine the microstructure of materials, the field-emission scanning electron microscopy (ZSEM, Zeiss Gemini SEM 500) was used. The transmission electron microscopy (TEM) picture of compounds was performed with JEOL-JEM-2100 Plus. X-ray photoelectron spectroscopy was employed to determine the elemental composition and chemical states (Thermo Fisher ESCALAB Xi^+). The elements of composites were examined by energy dispersive spectrometry (EDS) during measurement of FESEM system with the acceleration voltage of 15 kV.

2.3. Gas sensor fabrication and response measurements

The prepared SnS_2/graphene samples (20 mg) were added into 100 μL of DI water to obtain the suspension. After that, the prepared suspension was coated onto commercial gold electrode. Finally, the prepared sensing device was aged at 25 ℃ for one night. For

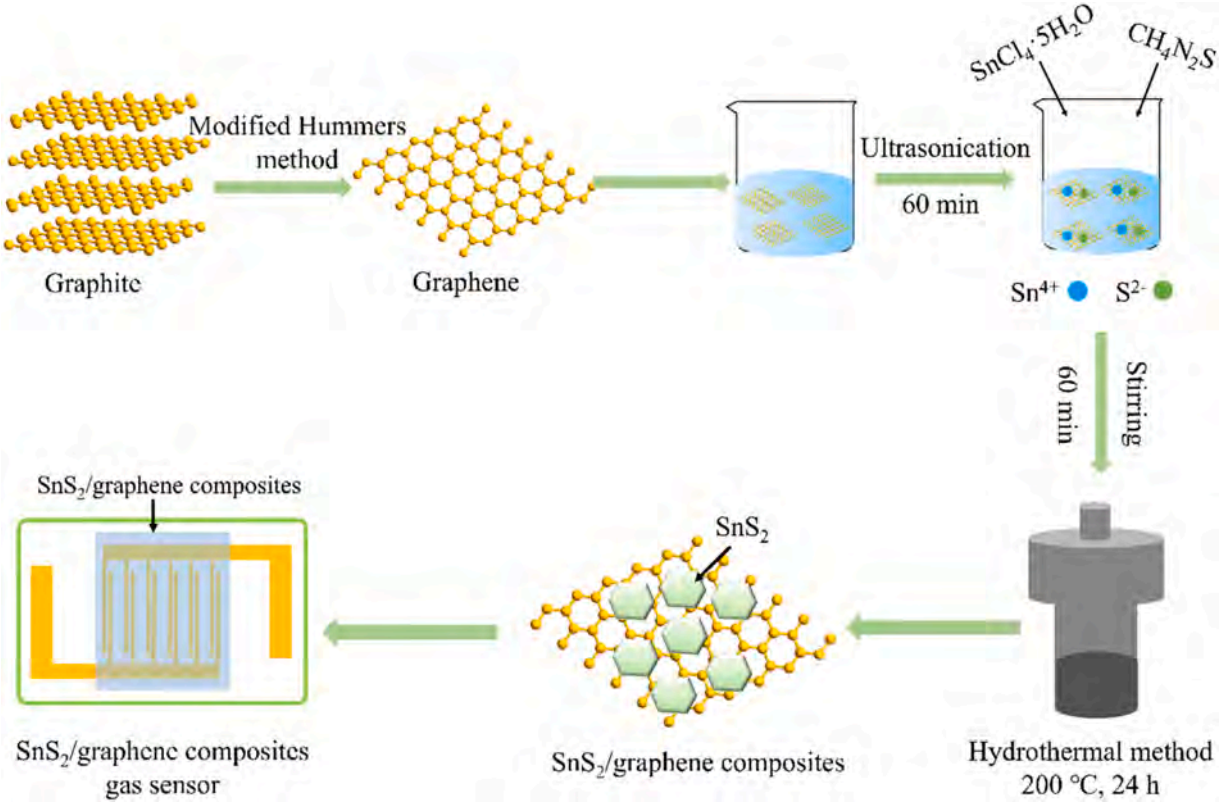

Fig. 1. Schematic diagram of the preparation of SnS_2 and graphene composites.

comparison, pure graphene and SnS_2-based sensors were fabricated by the similar method. The NH_3 sensing properties were determined by the static testing system (CGS-8HP). During measurement, the NH_3 gas was obtained by vaporizing organic ammonia solution (25 *wt*%). The concentration (C_g, ppm) of NH_3 was calculated by Eq. (1):

$$C_g = \frac{\rho \times C_L \times V_L}{M_o \times V_C} \quad (1)$$

where, the density of liquid is represented as ρ (g/cm^3), C_L is the concentration of liquid (*wt*%), V_L and V_C are the volume of liquid and chamber (mL), respectively. The molar mass of organics is denoted by M_o (g/mol). The sensor response (S_g) is defined $S_g = \frac{R_a - R_g}{R_a} \times 100\%$, where R_a and R_g were the resistance of sensor in air and target gas at RT (25 °C), respectively. The response (τ_{res}) and recovery time (τ_{rec}) were defined as time needed for achieving 90 % of maximum resistance change after injecting and exhausting target gas, respectively.

2.4. DFT calculations

In the process of Density-functional theory (DFT) calculation, the Vienna Ab initio Simulation Program (VASP) was performed. The Perdew–Burke–Ernzerhof (PBE) was used as exchange correlation potential for all calculations [19–21]. The plane-wave cutoff energy was fixed to 500 eV. The Hellmann-Feynman forces and energy convergence were set as 5×10^{-2} eV/$\dot{A}$ and 10^{-4} eV, respectively. The Monkhorst-pack k-point grids were set as $5 \times 5 \times 1$ and $7 \times 7 \times 1$ for structure optimization and density of states, respectively. The thickness of vacuum layer is set as 10 $\dot{A}$. The adsorption energy (E_{ads}) was calculated as:

$$E_{ads} = E_{Sensor+NH_3} - E_{Sensor} - E_{NH_3} \quad (2)$$

where$E_{Sensor+NH_3}$, E_{Sensor}, and E_{NH_3} are the total energy of sensor with adsorbed NH_3, pure sensor and NH_3 molecule, respectively.

3. Results and discussion

3.1. Materials characterization

The structure of SnS_2 and SnS_2/graphene composites is determined by X-ray diffraction (XRD). In Fig. 2, the peaks at about 15.01°, 28.19°, 32.24°, 41.87°, 49.98°, 52.51°, 55.06°, 60.63°, 67.39°, 70.61°, 84.63°, and 88.35° can be indexed to the (001), (100), (101), (102), (110), (111), (103), (201), (202), (113), (114), and (105) crystal planes of hexagonal SnS_2 (No. 23–0677). While, the characteristic peaks of graphene are not detected in the composites. The Raman spectra of SnS_2, graphene, and composites is depicted in Fig. 3. The Raman peaks at about 1354.93 cm^{-1} and 1592.4 cm^{-1} correspond to the D and G bands of graphene, imparting information about defects originating from functional groups and scattering of C in graphene, respectively [22,23]. In composites, the intensity ratio of D to G is about 0.89, which is higher than that of pure graphene (0.29), suggesting more surface defects caused by SnS_2. The Raman peak at about 313.45 cm^{-1} is ascribed to SnS_2, thus confirming that the compounds of SnS_2 and graphene are successfully prepared [24].

The morphologies of pristine SnS_2 and SnS_2/graphene composites are examined by SEM and TEM. Fig. 4a and b show that SnS_2 is composed of hexagonal nanosheets. Because of the non-uniformity of precursor and nanosheet damage during hydrothermal preparation, some irregular SnS_2 nanosheets are formed. Fig. 4(c-e) display the SEM morphology of SnS_2 and graphene composites, revealing that the SnS_2 nanosheets are confined to the graphene surface and that graphene is a suitable substrate for the nucleation and growth of SnS_2 nanosheets. Fig. 4(f-i) present the EDS maps showing that S, Sn, and C are evenly distributed and the formation of SnS_2 and graphene heterojunction. The TEM images in Fig. 5(a-c) behave the hexagonal SnS_2 nanosheets were formed during hydrothermal method and lattice spacing is about 0.58 nm, which is corresponded to the (001) facet of SnS_2. Fig. 5d and e display the TEM images of SnS_2 and graphene composite, revealing the hexagonal SnS_2 nanosheets are decorated on graphene. Graphene with a large specific surface area provides abundant nucleation sites for SnS_2 nanosheets. The detailed microstructure is investigated by high-resolution TEM, and Fig. 5f shows the interplanar spacing of 0.58 nm for the (001) plane of hexagonal SnS_2.

Fig. 6a displays the S 2*p* XPS spectrum of pure SnS_2. The two peaks at about 161.48 eV and 163.21 eV are assigned to S $2p_{3/2}$ and S $2p_{1/2}$, respectively. The Sn 3*d* spectrum of pure SnS_2 in Fig. 6b shows peaks at about 486.65 eV and 495.16 eV for Sn $3d_{5/2}$ and Sn $3d_{3/2}$, respectively. Fig. 6c displays the survey spectrum of SnS_2/graphene composite disclosing the presence of Sn, S, and C. The carbon peak in Fig. 6d shows the peak of 284.8 eV is attributabled to C-C of graphene and 286.85 eV for C-O bond. As displayed in Fig. 6e and f, the binding energies of S 2*p* (S $2p_{3/2}$ and S $2p_{1/2}$) and Sn 3*d* (Sn $3d_{5/2}$ and Sn $3d_{3/2}$) increase to 161.76 eV, 163.98 eV, 487.32 eV, and 495.87 eV, respectively, implying loss of outer electrons and that SnS_2 and graphene have distinct interfacial electron transfer between SnS_2 and graphene.

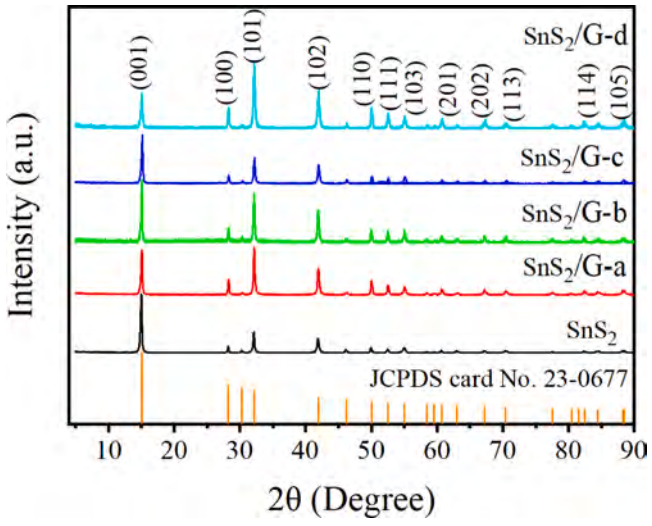

Fig. 2. XRD spectra of SnS_2, SnS_2/G-a, SnS_2/G-b, SnS_2/G-c, and SnS_2/G-d.

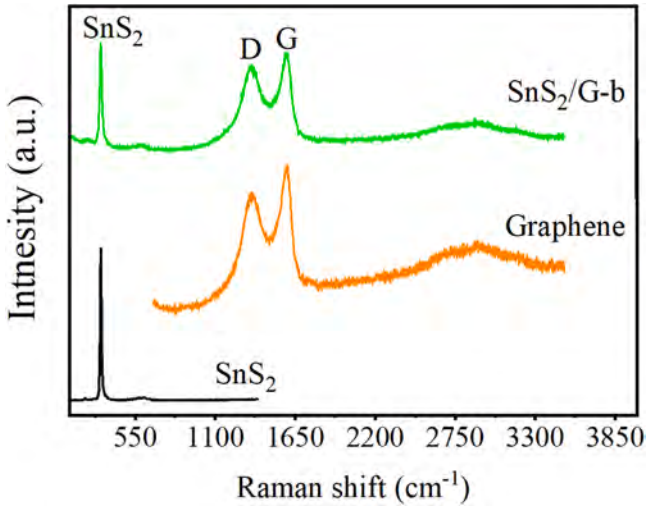

Fig. 3. Raman scattering spectra of SnS_2, graphene, and SnS_2/graphene (Ce-Mo-b).

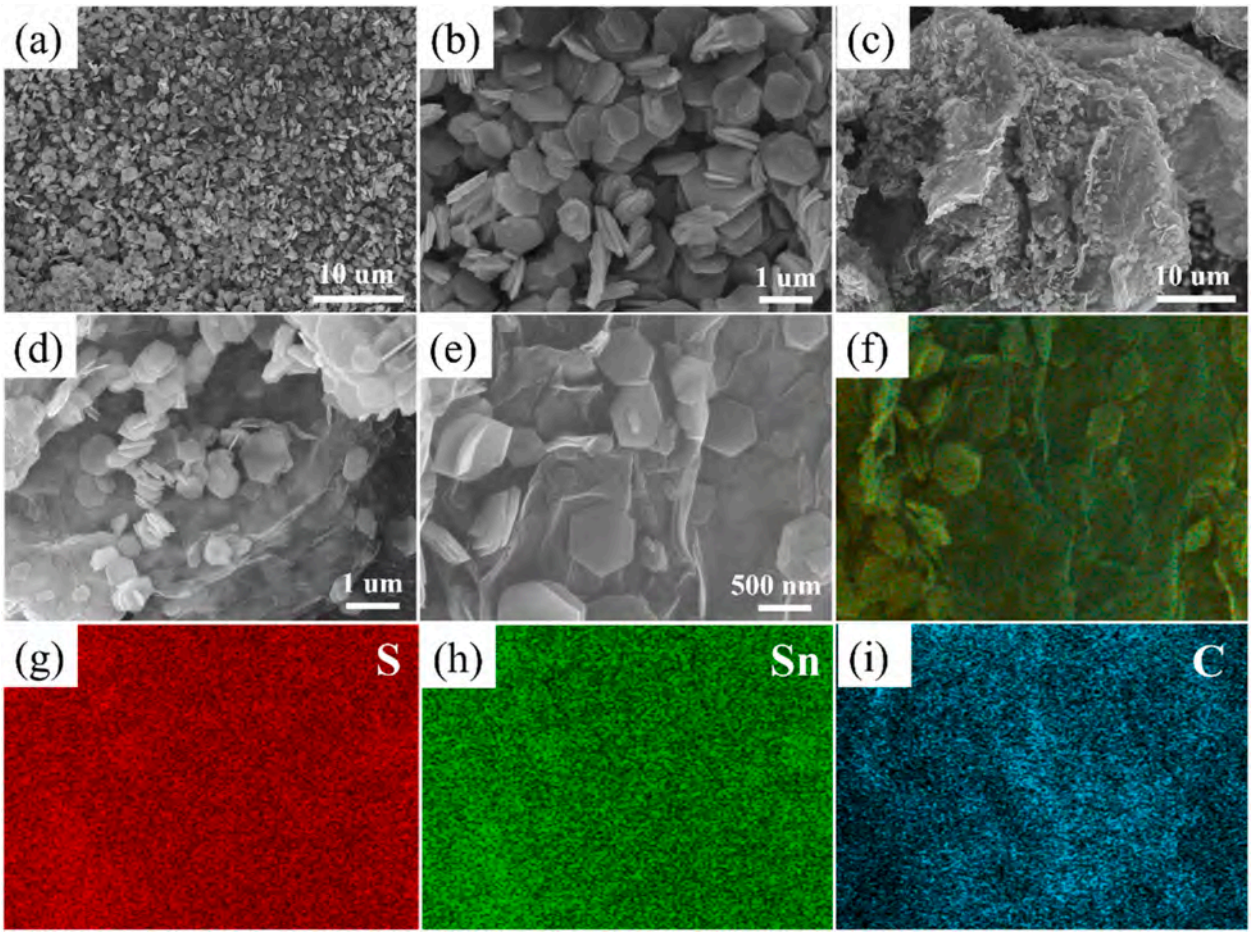

Fig. 4. SEM images of (a-c) SnS_2 and (d, e) SnS_2/graphene (SnS_2/G-b), (f-i) EDS elemental maps of the SnS_2 and graphene composite (SnS_2/G-b).

3.2. Sensing properties

The NH_3 sensing properties of pristine SnS_2, graphene, and SnS_2/graphene composites are investigated at RT. Fig. 7a presents the responses to 500 ppm NH_3, revealing responses of 5.28 % and 58.93 % for graphene and SnS_2, respectively. In comparison, the response of composite is enhanced with SnS_2/G-b showing 1.5-fold and 17-fold improvement over the pristine SnS_2 and graphene, respectively. With increasing graphene amounts, the response increases initially and then decreases, and that of SnS_2/G-b is the optimal sensor. Based on the results of Nitrogen adsorption-desorption experiments, the Brunauer-Emmett-Teller (BET) surface area of SnS_2 is about 12.1912 m^2/g (Fig. S1a). When composited with 0.4 *wt*% graphene, the BET surface area is increased to 91.4592 m^2/g (Fig. S1b). And thus the NH_3-sensing response is enhanced. While if the graphene content is increased further, the BET surface area is reduced (Figure S1c and d). Hence, the room-temperature NH_3-sensing response becomes poor at high content of graphene. Fig. 7(b-d) display the resistance change curves of graphene, SnS_2, and SnS_2/G-b to different concentrations of NH_3 at RT. The resistance of graphene increases immediately upon exposure to NH_3 and then stabilizes, suggesting that graphene has p-type semiconducting properties. Upon exposure to air, the resistance of graphene can't recover to its initial value (Fig. 7b), whereas for pure SnS_2, the resistance decreases immediately showing n-type semiconducting characteristics. During exposure to air, the resistance couldn't completely recover to the initial state (Fig. 7c). In comparison, the resistance of SnS_2 and graphene composite decreases showing the n-type semiconducting behavior, and upon air exposure, the resistance recovers to the initial value (Fig. 7d). The response time of SnS_2/G-b decreases from 31 s to 23 s when the NH_3 concentration is added from 50 to 500 ppm. At the same time, the recovery time increases from 435 s to 1427 s (Fig. 7e). Fig. 7f presents the NH_3 concentration versus response relationship of SnS_2/G-b. At concentrations between 1 and 50 ppm, the response improves evidently. More importantly, a linear relationship is observed between the response and NH_3 concentration with the correlation coefficient R^2 of 0.99. The response of SnS_2/G-b is enhanced by 1.01472 % when the NH_3 concentration is increased by 1 ppm at RT. At concentrations between 100 and 500 ppm, the response improves slowly at RT, only by 0.039 % when the NH_3 concentration is increased by 1 ppm at RT. At low concentrations, the current is directly proportional to the NH_3 concentration because most of the sites are available, but at high NH_3 concentrations, these active sites are all occupied by NH_3 thus reaching a steady state [25–27]. The detection limit (*DL*) is calculated by Eq. (3) [27]:

$$DL = 3 \times \frac{RMS}{Slope} \tag{3}$$

where *RMS* represents the root-mean-square of noise, and the slope is calculated from the linear response between 1 and 50 ppm NH_3. The *DL* of SnS_2/G-b sensor is about 0.1 ppm, that is below the typical ammonia concentration (1 ppm) in exhaled air from patients with kidney diseases boding well for early diagnosis and prevention of kidney diseases [11]. Fig. 7g shows the resistance changes of SnS_2/G-b to 100 ppm NH_3 for five successive cycles revealing good repeatability and reversibility. The long-term stability of SnS_2/G-b is evaluated by recording the room-temperature response to 100 ppm NH_3 under 48 % RH for 15 days. The test was repeated for three cycles. In Fig. 7h, a slight change in baseline resistance was observed, which subsequently stabilized again.

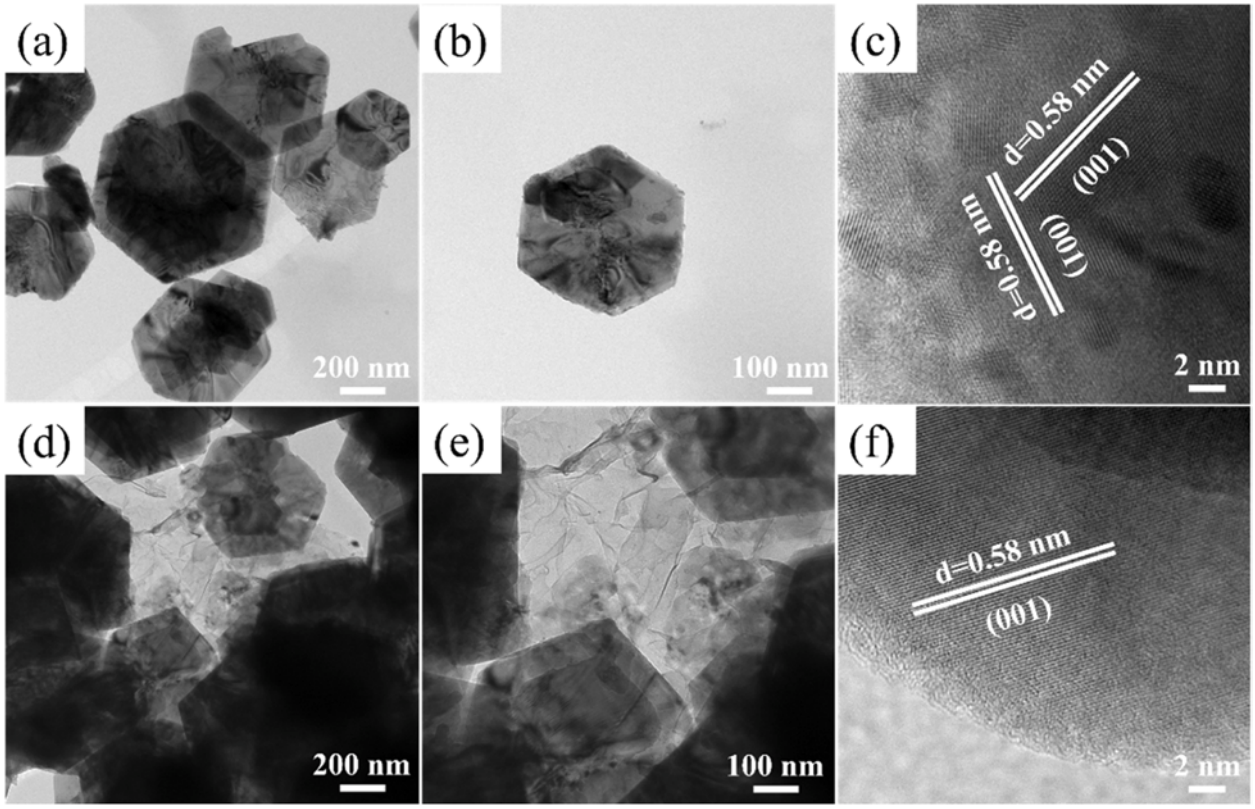

Fig. 5. TEM images of (a-c) SnS_2 and (d, e) SnS_2/graphene (SnS_2/G-b).

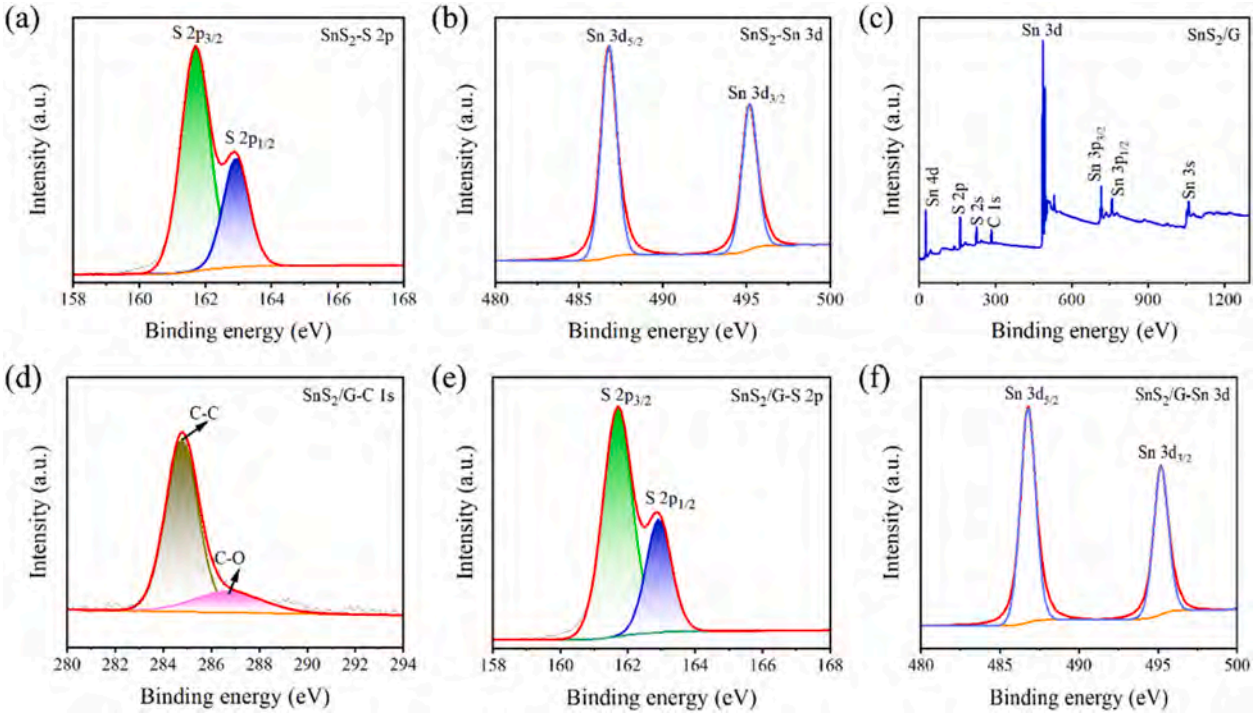

Fig. 6. (a) XPS S 2*p* and (b) Sn 3*d* spectra of SnS_2; (c) Survey, (d) C 1 *s*, (e) S 2*p*, (f) and Sn 3*d* spectra of SnS_2/graphene (SnS_2/G-b).

The relative standard deviation (RSD) of resistance and response was about 3.53 % and 8.95 %, respectively. Additionally, the response after 15 days decreases by only 16.67 %, behaving the better stability. Good selectivity is also crucial, and the room-temperature response of SnS_2/G-b sensor to 100 ppm NH_3, C_3H_6O, C_2H_5OH, CH_3OH, C_3H_8O, NO_2, H_2S and CO is shown in Fig. 7i. The response to C_3H_6O, C_2H_5OH, CH_3OH, C_3H_8O, H_2S, CO and NO_2 are about 2.81 %, 4.51 %, 3.16 %, 6.18 %, 5.28 %, 2.36 % and 17.83 %, respectively. The SnS_2/G-b sensor is slightly sensitive to NO_2, While the response is still much smaller than that of NH_3 (62.36 %) and the resistance couldn't recovery to initial

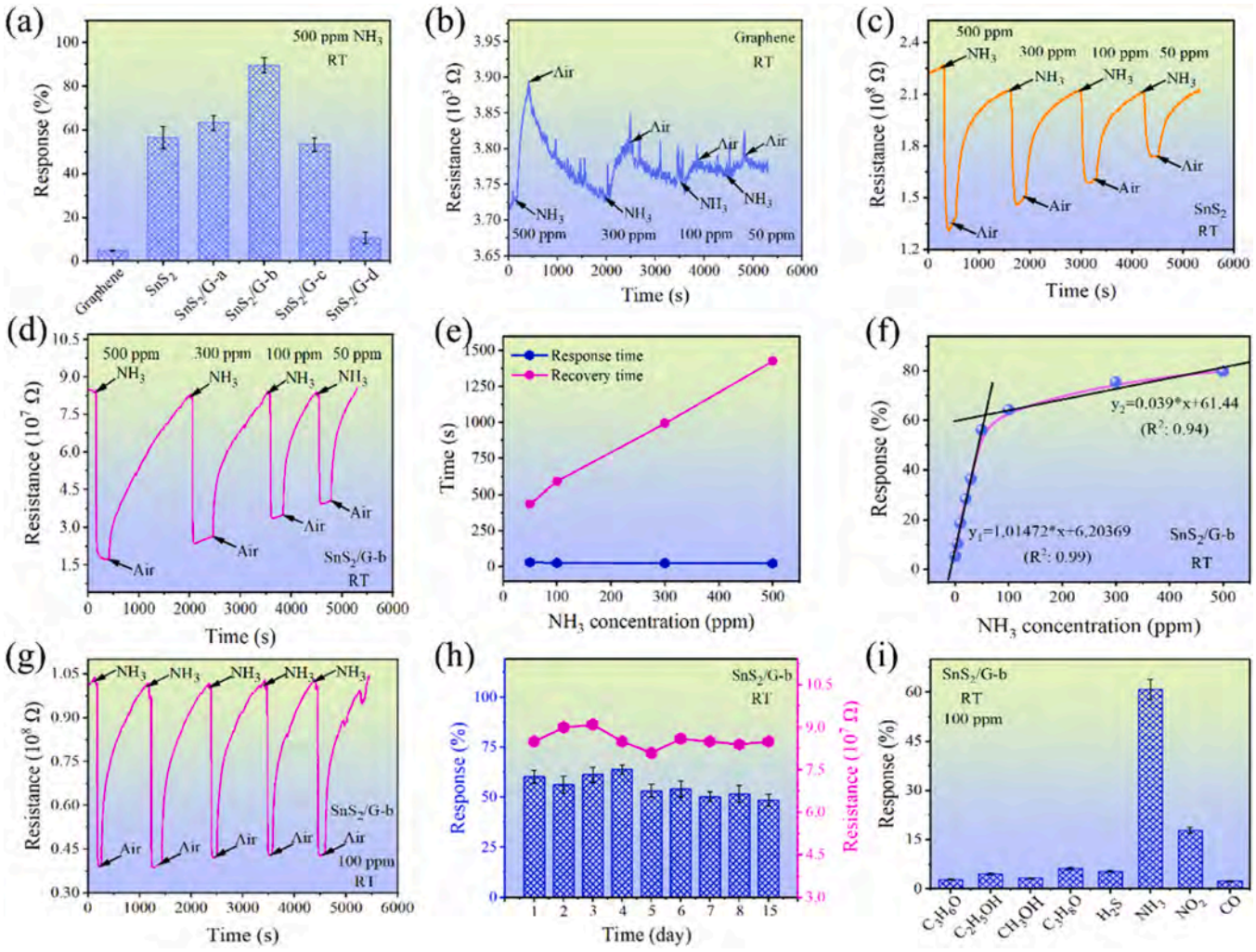

Fig. 7. (a) Response of graphene, SnS_2, and SnS_2/graphene; Real-time resistance variations of (b) Graphene, (c) SnS_2, and (d) SnS_2/G-b to 50–500 ppm NH_3 at RT; (e) Response and recovery time of SnS_2/G-b to 50–500 ppm NH_3 at RT; (f) Response of SnS_2/G-b to 1–500 ppm NH_3 at RT; (g) Five cycle repeatability of SnS_2/G-b to 100 ppm NH_3 at RT; (h) The response (left) and base resistance (right) of SnS_2/G-b to 100 ppm NH3 for 15 days at RT; (i) Selectivity of SnS_2/G-b for NH_3 at RT.

value, behaving the poor recovery performance for NO_2 (Fig. S2). Hence, the composites behave the excellent selectivity to NH_3 at RT.

The sensing properties of SnS_2/G-b at different temperatures and relative humidity are investigated. As shown in Fig. 8a, as the temperature goes up from 23 to 132 ℃, the response diminishes from 28.36 % to 1.03 %. The response is decreased by 0.566 % as the working temperature is added by 1 ℃, which is equal to decrease of 557.78 ppb NH_3 at RT. A higher temperature leads to faster desorption. The time for NH_3 to react with SnS_2/graphene compounds is not enough, resulting in poor response [26–28]. In addition, at higher temperature, the baseline resistance also decreases. At higher temperature, the more electrons form valence band are excited into conduction band and thus the

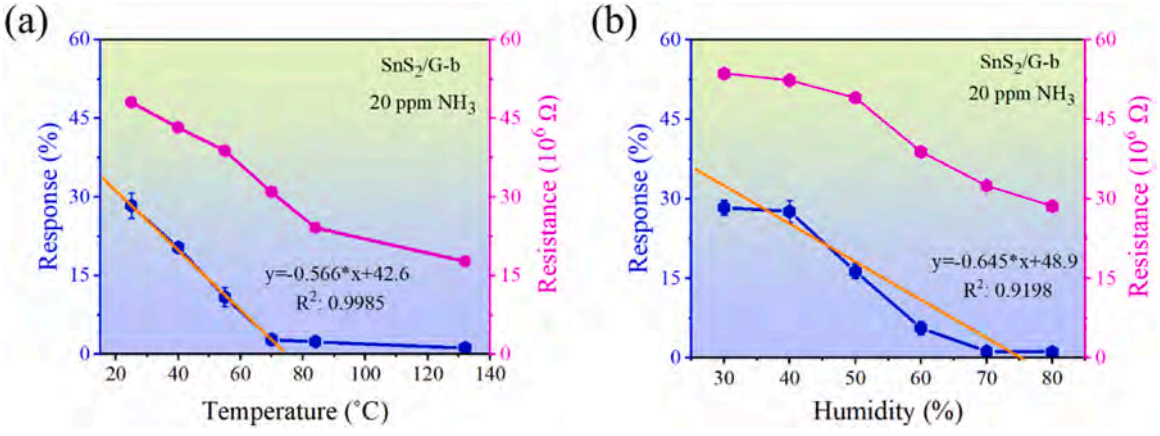

Fig. 8. The response (left) and baseline resistance (right) of SnS_2/G-b to 20 ppm NH_3 under different (a) Temperature and (b) Relative humidity.

concentration of electrons is increased, resulting in the decrease of resistance [26–28]. Fig. 8b shows the baseline resistance and NH_3 response of SnS_2/G-b under different environmental humidity (RH). With increasing RH, the baseline resistance and response decreases. The response to 20 ppm NH_3 is decreased by 0.645 % as the RH is added by 1 %, which is equal to decrease of 635.64 ppb NH_3 at RT. At high RH, H_2O molecules in air absorb onto the surface. The OH^- of H_2O may dissociate and become an electron donor to transfer electrons to conduction band of materials and thus the resistance is decreased [29,30]. Additionally, the water molecules inhibit the adsorption ability of NH_3, leading to poor response. In addition, the comparison of NH_3 sensing properties of sensors in this work with those in the previous work is presented in Table S1 [8,31–35]. The response of SnS_2 and SnS_2/ZnS composites is much higher than that of SnS_2/graphene composites in this work. While, the working temperature is much higher (>100 ℃) [8, 31]. The pure SnO_2 behaves no response to NH_3 at RT [32]. For the WS_2 [33], $Ti_3C_2T_x$ [34], SnO_2/SnS_2 [32] and ZnO/$Ti_3C_2T_x$ [35], the working temperature is RT. However, the response is poorer in comparison with this work. Hence, the SnS_2/graphene composites in this work behave the excellent room-temperature NH_3-sensing performance.

3.3. Sensing mechanism

The superior RT NH_3 sensing properties can be explained by three factors of strong adsorption ability of SnS_2, high carrier mobility of graphene, and heterojunction enhancement. In the first-principles calculation of Fig. 9, the adsorption energy of SnS_2 to NH_3 is much more negative than that of graphene, indicating SnS_2 has stronger adsorption ability for NH_3. Hence, when composite is exposed to a reducing gas like NH_3, NH_3 on the surface of SnS_2 releases electrons to the conduction band of SnS_2. The free electrons flow across the heterojunction to graphene, thereby reducing the resistance and yielding the n-type behavior (Fig. 10a and b).

Graphene plays a crucial role in enhancing the room-temperature NH_3 sensing response of SnS_2. During sample preparation, the oxygen-containing groups on graphene are negatively charged. The Sn^{4+} ions are attached to graphene, and then nucleation and growth of SnS_2 ensue *via* sulfidation of Sn^{4+}. Moreover, graphene increases the electrical conductivity and electron exchange with NH_3 molecules. Since graphene has a large surface area, NH_3 adsorption also increases. Finally, the interface between SnS_2 and graphene modulates charge transfer as shown by our first-principles calculation.

To reveal the sensing mechanism of sensor toward C_3H_6O, C_2H_5OH,

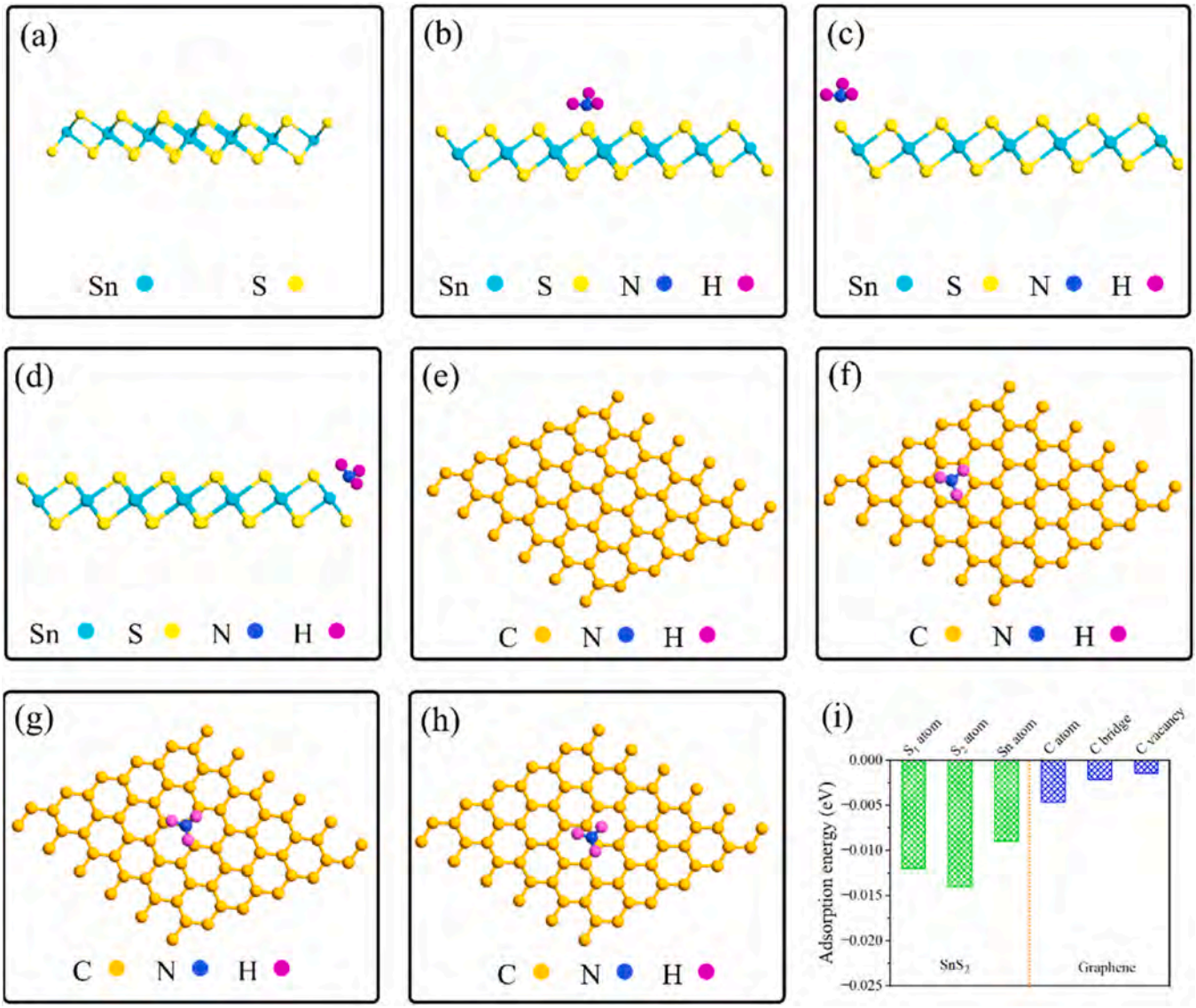

Fig. 9. Side views of (a) SnS_2, (b-d) SnS_2 adsorbing NH_3, (e) Graphene, (f-h) graphene adsorbing NH_3, and (i) Adsorption energies of SnS_2 and graphene for NH_3.

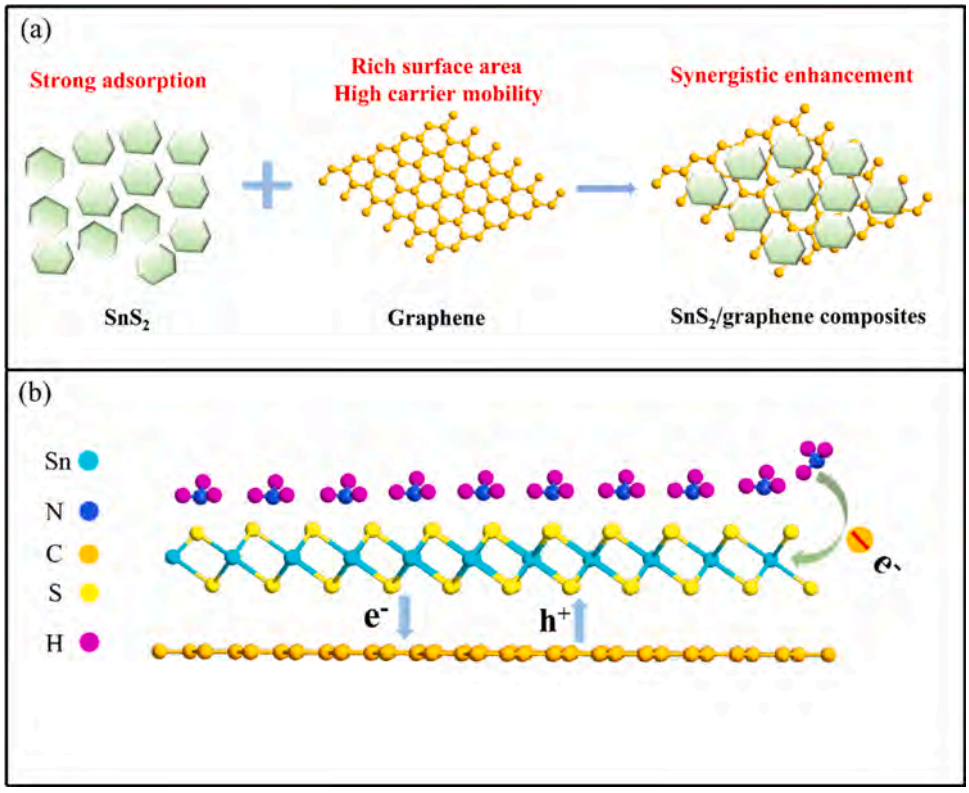

Fig. 10. (a) Schematic illustration of the sensing mechanism of the SnS_2 and graphene composite; (b) Schematic diagram of NH_3 adsorption on the composite.

CH_3OH, H_2S and NH_3, the room-temperature response of SnS_2/G-b sensor to 100 ppm of C_3H_6O, C_2H_5OH, CH_3OH, H_2S and NH_3 in N_2, air and O_2 are measured, respectively. As presented in Fig. 11 (a-e), the response to C_3H_6O, C_2H_5OH, CH_3OH, H_2S and NH_3 is not enhanced obviously in O_2 compared to that in N_2. In N_2, almost no O_2 is adsorbed on the surface of sensor and few O_2^- ions are formed. The C_3H_6O, C_2H_5OH, CH_3OH, H_2S and NH_3 molecular directly release electrons to sensor causing reduced resistance. In O_2, abundant O_2 are adsorbed on

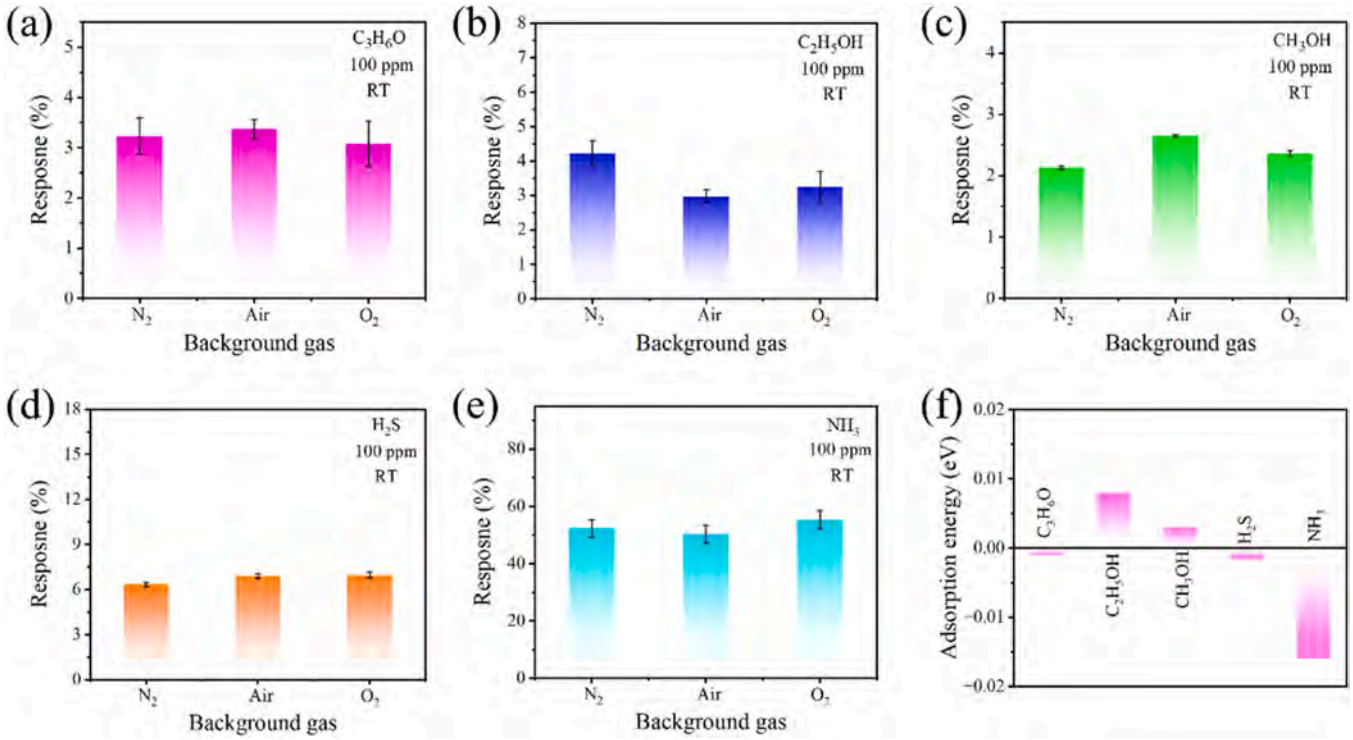

Fig. 11. The response of SnS_2/graphene (SnS_2/G-b) sensor toward 100 ppm of (a) C_3H_6O, (b) C_2H_5OH, (c) CH_3OH, (d) H_2S and (e) NH_3 at RT in the different background gas of N_2, air and O_2. (f) The adsorption energy of SnS_2 toward C_3H_6O, C_2H_5OH, CH_3OH, H_2S and NH_3.

the surface of sensor and lots of O_2^- ions are formed. Surprisingly, the response is not enhanced obviously. It confirms that the resistance variation is mainly relied on the direct electron transfer between gas molecular (C_3H_6O, C_2H_5OH, CH_3OH, H_2S and NH_3) and SnS_2/graphene composites sensor. In addition, the adsorption energy of C_3H_6O, C_2H_5OH, CH_3OH, H_2S and NH_3 on the surface of SnS_2 is calculated and displayed in Fig. 11**f**. It's found that the SnS_2 behaves the highest adsorption ability to NH_3 in comprimario with other gas. The more electrons are released from NH_3 to SnS_2, behaving the excellent selectivity to NH_3 at RT.

To further reveal the dependence between heterojunction and sensing response, the work functions of SnS_2 and graphene are derived and displayed in Fig. 12a. The work function of SnS_2 is 4.4 eV, which is lower than that of graphene (4.6 eV). In the composite, free electrons move from SnS_2 to graphene until the Fermi levels of SnS_2 and graphene reach a balance, consequently forming a heterojunction. As shown in Fig. 12b, the structure of SnS_2 bends upward, and diffusion and drift of charge carriers create a depletion zone at interface. Oxygen absorbs onto the surface to form O_2^-. The electron potential is shifted upward and thus the space charge region is broadened, inhibiting the electron transfer (Fig. 12c). When NH_3 molecules adsorb onto the active sites, the electron of NH_3 is transferred to sensor, thus changing the electron potential. The barrier shifts downward to narrow the space charge region and allow electrons to pass more easily (Fig. 12d). The current across the SnS_2/graphene p-n junction obeys the thermionic emission model expressed by Eq. 4: [36]

$$I = AA^*T^2\exp\left(-\frac{e\varphi_{SBH}}{kT}\right)\left[\exp\left(\frac{eV}{nKT}\right)-1\right] \quad (4)$$

Since NH_3 is a reducing gas, it has a strong electron donation ability. After adsorbing onto SnS_2, NH_3 molecules donate electrons to the conduction band of SnS_2, and the electron concentration increases and the resistance decreases. The SnS_2 and graphene interface modifies the junction potential and the sensitive ability to NH_3 is obviously enhanced [29,30].

The total and partial density of states of SnS_2, graphene, and composites are also derived and displayed in Fig. 13. The bandgap of SnS_2 is about 2.1 eV. The bottom of conduction band (CB) and the top of valence band (VB) are mainly associated with the Sn *d* and S *p* orbitals, respectively (Fig. 13a-c). The electrons in VB isn't easily jumped to CB, behaving the poor conductivity at RT. As for graphene, the bandgap is zero. The bottom of CB and top of VB is overlapped at Fermi level, behaving as a metal (Fig. 13d-f). In Fig. 13(g-i), the bandgap of SnS_2 and graphene heterojunction is about 0.28 eV. The bottom of CB and top of VB are mainly related to the C *p* and Sn *d* orbitals, respectively. Electrons can more easily jump from VB to CB, thus behaving the excellent conductivity and better NH_3 response at RT.

4. Conclusion

Heterostructure SnS_2 and graphene composites are prepared hydrothermally. Compared to pure SnS_2 and graphene, the SnS_2 and graphene composites have excellent responses to ppm level NH_3 under ambient conditions, such as high response, short response and recovery times, long-term stability, and low detection limit of 0.1 ppm. Except for NH_3, the composite is also slightly sensitive to NO_2. The room-temperature response to 100 ppm NO_2 is only about 17.83 %, which is much smaller than that of NH_3 (62.36 %) and the resistance couldn't recovery to initial value, behaving the poor recovery performance for NO_2. Hence, the composites also behave the excellent selectivity to NH_3 at RT. DFT calculations disclose that the improved room-temperature NH_3-sensing response stem from stronger NH_3 adsorption of SnS_2, higher carrier mobility of graphene, and more effective charge transfer at interface. The results enrich our understanding of the detection and enhancement mechanisms, and the outstanding sensing properties suggest a large potential in sensing applications.

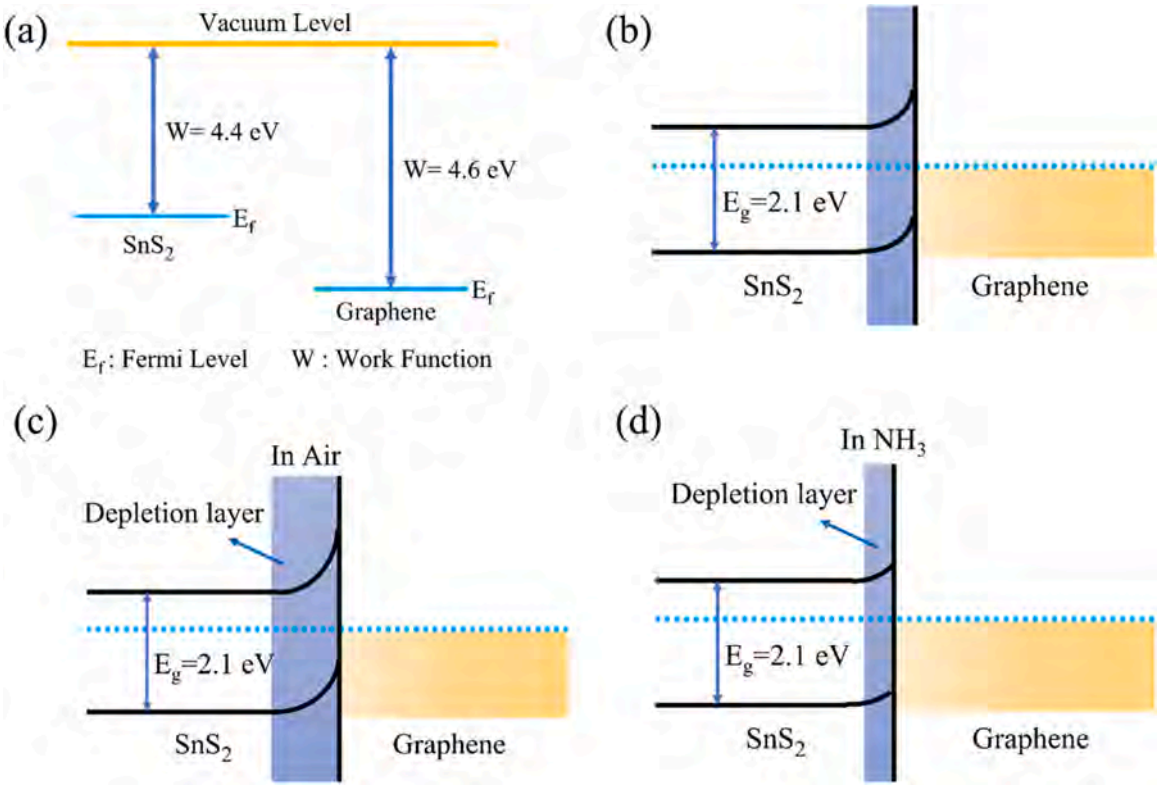

Fig. 12. (a) Work functions of SnS_2 and graphene; Energy band diagrams of the heterojunction: (b) Vacuum, (c) Air, and (d) NH_3.

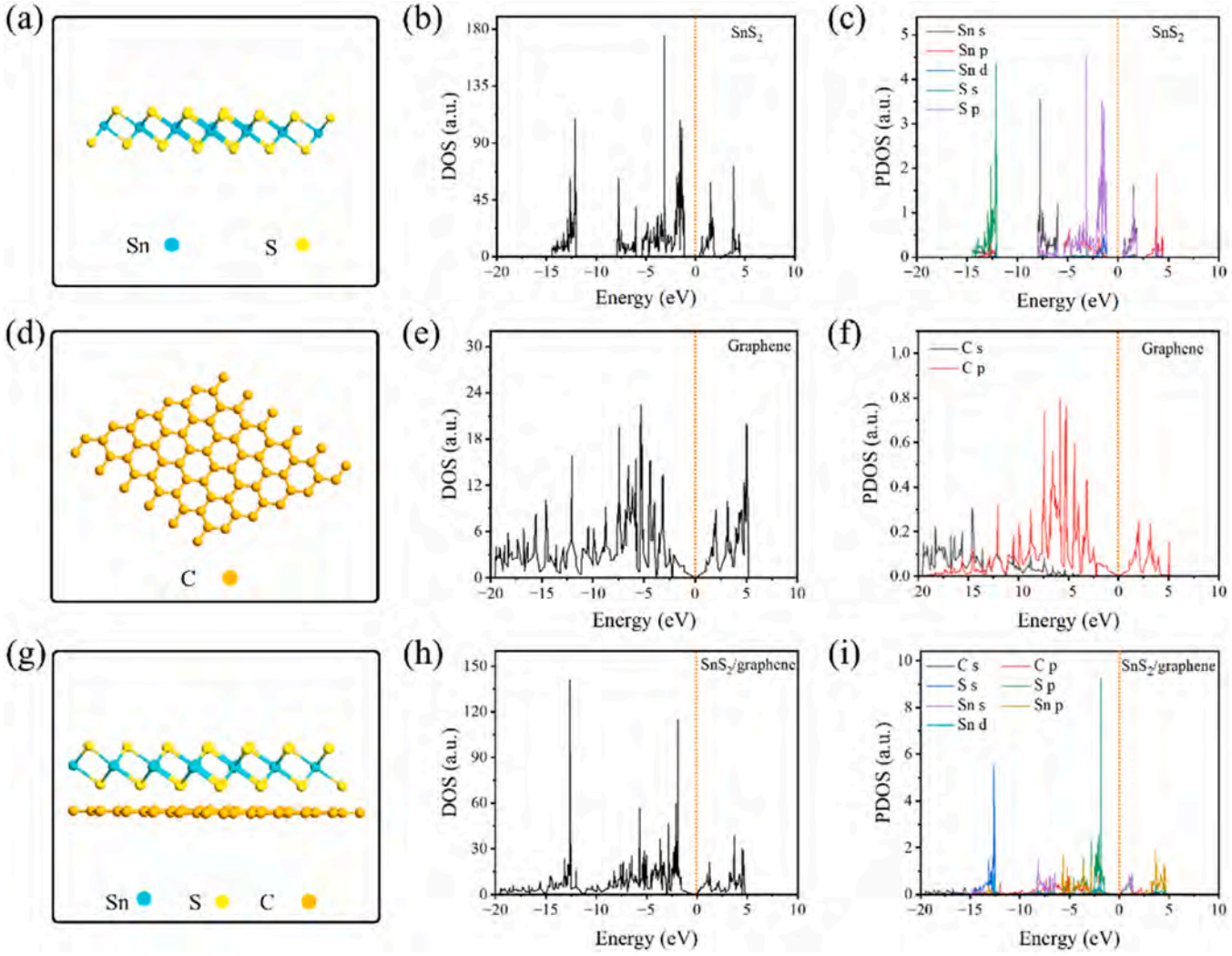

Fig. 13. Atomic structure, DOS, and PDOS of (a-c) SnS_2, (d-f) graphene, and (g-i) SnS_2/graphene heterojunction.

CRediT authorship contribution statement

Lei Xinyu: Formal analysis, Data curation, Conceptualization. **Xu Jiayuan:** Supervision, Software, Formal analysis. **Sun Henghui:** Resources, Project administration, Methodology. **Zhang Dr. Lizhai:** Writing – review & editing, Writing – original draft, Validation, Supervision, Investigation. **Ma Fei:** Writing – review & editing, Writing – original draft, Supervision, Software. **Ai TaoTao:** Investigation, Funding acquisition, Formal analysis. **Chu Paul K:** Formal analysis, Data curation, Conceptualization.

Declaration of Competing Interest

The authors declare that they have no known competing financial interests or personal relationships that could have appeared to influence the work reported in this paper.

Acknowledgments

This work was jointly supported by Natural Science Foundation of Shaanxi Province (2023-JC-QN-0476), Shaanxi University of Technology Research Grant (no. SLGRCQD2207), Scientific research project of Shaanxi Provincial Education Department (no.23JK0375), Science and technology program for overseas students of Shaanxi province (2023016), and City University of Hong Kong Donation Research Grants (DON-RMG no.9229021 and 9220061).

Appendix A. Supporting information

Supplementary data associated with this article can be found in the online version at doi:10.1016/j.snb.2025.137565.

Data availability

No data was used for the research described in the article.

References

[1] Q.N. Pan, T.T. Li, D.Z. Zhang, Ammonia gas sensing properties and density functional theory investigation of coral-like Au-$SnSe_2$ Schottky junction, Sens. Actuators B Chem. 332 (2021) 129440.
[2] X. Tian, L.J. Yao, X.X. Cui, R.J. Zhao, T. Chen, X.C. Xiao, Y.D. Wang, A two-dimensional $Ti_3C_2T_X$ MXene@TiO_2/MoS_2 heterostructure with excellent selectivity for the room temperature detection of ammonia, J. Mater. Chem. A 10 (2022) 5505–5519.
[3] W.X. Wang, Y.H. Zhen, J.Y. Zhang, Y.D. Li, H. Zhong, Z.L. Jia, Y. Xiong, Q.Z. Xue, Y.G. Yan, N.S. Alharbi, T. Hayat, SnO_2 nanoparticles-modified 3D-multilayer MoS_2 nanosheets for ammonia gas sensing at room temperature, Sens. Actuators B Chem. 321 (2020) 128471.
[4] Q.X. Feng, B.Y. Huang, X.G. Li, Graphene-based heterostructure composite sensing materials for detection of nitrogen-containing harmful gases, Adv. Funct. Mater. 31 (2021) 2104058.
[5] V. Chaudhary, N. Ashraf, M. Khalid, R. Walvekar, Y. Yang, A. Kaushik, Y.K. Mishra, Emergence of MXene–polymer hybrid nanocomposites as high-performance next-

generation chemiresistors for efficient air quality monitoring, Adv. Funct. Mater. 32 (2022) 2112913.
[6] Z.Y. Qin, K. Xue, H.C. Yue, H. Wang, J. Zhang, C. Ouyang, C.S. Xie, D.W. Zeng, Enhanced room-temperature NH_3 gas sensing by 2D SnS_2 with sulfur vacancies synthesized by chemical exfoliation, Sens. Actuators B Chem. 262 (2018) 771–779.
[7] X. Li, W. Zeng, S.J. Zhuo, B.W. Qian, Q. Chen, Q. Luo, R. Qian, Highly sensitive room-temperature detection of ammonia in the breath of kidney disease patients using $Fe_2Mo_3O_8/MoO_2$@MoS_2 nanocomposite gas sensor, Adv. Sci. 11 (2024) 2405942.
[8] Y. Xiong, W.W. Xu, D.G. Ding, W.B. Lu, L. Zhu, Z.Y. Zhu, Y. Wang, Q.Z. Xue, Ultra-sensitive NH_3 sensor based on flower-shaped SnS_2 nanostructures with sub-ppm detection ability, J. Hazard. Mater. 341 (2018) 159–167.
[9] B. Zhang, Y.D. Liu, T.T. Liang, T. Sakthivel, L.M. Yu, Z.F. Dai, Activating the basal plane of defective SnS_2 nanosheets for NH_3 gas sensing, ACS Appl. Nano Mater. 3 (2020) 4642–4653.
[10] H.W. Chen, Y.T. Chen, H. Zhang, D.W. Zhang, P. Zhou, J. Huang, Suspended SnS_2 layers by light assistance for ultrasensitive ammonia detection at room temperature, Adv. Funct. Mater. 28 (2018) 1801035.
[11] T.T. He, S.P. Sun, B.Y. Huang, X.G. Li, MXene/SnS_2 heterojunction for detecting sub-ppm NH_3 at room temperature, ACS Appl. Mater. Interfaces 15 (2023) 4194–4207.
[12] J.Z. Bai, Y.B. Shen, S.K. Zhao, A. Li, Z.K. Kang, B.Y. Cui, D.Z. Wei, Z.Y. Yuan, F. L. Meng, Room-temperature NH_3 sensor based on SnO_2 quantum dots functionalized SnS_2 nanosheets, Adv. Mater. Technol. 8 (2023) 2201671.
[13] P.K. Mishra, H.J. Choi, J.W. Ryu, G.J. Choi, V. Kumar, P. Kumar, J. Singh, S. Kumar, J.S. Gwag, Recent progress in gas sensing based on 2D SnS_2 and its heterostructure platforms: a review, Sens. Actuator A Phys. 365 (2024) 114850.
[14] E. Lee, Y.S. Yoon, D.J. Kim, Two-dimensional transition metal dichalcogenides and metal oxide hybrids for gas sensing, ACS Sens 3 (2018) 2045–2060.
[15] D.J. Buckley, N.C.G. Black, E.G. Castanon, C. Melios, M. Hardman, O. Kazakova, Frontiers of graphene and 2D material-based gas sensors for environmental monitoring, 2D Mater. 7 (2020) 032002.
[16] F. Schedin, A.K. Geim, S.V. Morozov, E.W. Hill, P. Blake, M.I. Katsnelson, K. S. Novoselov, Detection of individual gas molecules adsorbed on graphene, Nat. Mater. 6 (2007) 652–655.
[17] C. Gomez-Navarro, R.T. Weitz, A.M. Bittner, M. Scolari, A. Mews, M. Burghard, K. Kern, Electronic transport properties of individual chemically reduced graphene oxide sheets, Nano Lett. 7 (2007) 3499–3503.
[18] D.C. Marcano, D.V. Kosynkin, J.M. Berlin, A. Sinitskii, Z. Sun, A. Slesarev, L. B. Alemany, W. Lu, J.M. Tour, Improved synthesis of graphene oxide, ACS Nano 4 (2010) 4806–4814.
[19] G. Kresse, J. Furthmuller, Efficient iterative schemes for ab initio total-energy calculations using a plane-wave basis set, Phys. Rev. B: Condens. Matter Mater. Phys. 54 (1996) 11169–11186.
[20] G. Kresse, J. Hafner, Ab initio molecular dynamics for open-shell transition metals, Phys. Rev. B: Condens. Matter Mater. Phys. 48 (1993) 13115–13118.
[21] G. Kresse, D. Joubert, From ultrasoft pseudopotentials to the projector augmented-wave method, Phys. Rev. B: Condens. Matter Mater. Phys. 59 (1999) 1758–1775.
[22] K. Krishnamoorthy, M. Veerapandian, R. Mohan, S.J. Kim, Investigation of Raman and photoluminescence studies of reduced graphene oxide sheets, Appl. Phys. A. 106 (2012) 501–506.
[23] D.X. Yang, A. Velamakanni, G. Bozoklu, S. Park, M. Stoller, R.D. Piner, S. Stankovich, J. Inhwa, D.A. Field, C.A. VentriceJr, R.S. Ruoff, Chemical analysis of graphene oxide films after heat and chemical treatments by X-ray photoelectron and Micro-Raman spectroscopy, Carbon 47 (2009) 145–152.
[24] J.Z. Ou, W. Ge, B. Carey, T. Daeneke, A. Rotbart, W. Shan, Y. Wang, Z. Fu, A. F. Chrimes, W. Wlodarski, S.P. Russo, Y.X. Li, K. Kalantar-Zadeh, Physisorption-Based Charge Transfer in Two Dimensional SnS_2 for selective and reversible NO_2 gas sensing, ACS Nano 9 (2015) 10313–10323.
[25] C.W. You, T. Fu, C.B. Li, X. Song, B. Tang, X. Song, Y. Yang, Z.P. Deng, Y.Z. Wang, F. Song, A latent-fire-detecting olfactory system enabled by ultrafast and sub-ppm ammonia-responsive $Ti_3C_2T_x$ MXene/MoS_2 sensors, Adv. Funct. Mater. 32 (2022) 2208131.
[26] H. Long, A. Harley-Trochimczyk, T. Pham, Z.R. Tang, T.L. Shi, A. Zettl, C. Carraro, M.A. Worsley, R. Maboudian, High surface area MoS_2/graphene hybrid aerogel for ultrasensitive NO_2 detection, Adv. Funct. Mater. 26 (2020) 5158–5165.
[27] L.T. Duy, D.J. Kim, T.Q. Trung, V.Q. Dang, B.Y. Kim, H.K. Moon, N.E. Lee, High performance three-dimensional chemical sensor platform using reduced graphene oxide formed on high aspect-ratio micro-pillars, Adv. Funct. Mater. 25 (2015) 883–890.
[28] F. Liu, J.B. Zhao, C.Z. Chen, H. Zhou, N. Xiang, Z.D. Jin, L. Liu, S.Q. Li, J.R. Liu, L. L. Wu, Dual enhancement in response and anti-humidity properties of a triethylamine sensor based on trimethoxypropylsilane self-assembled functionalized In_2O_3, Sens. Actuators B Chem. 417 (2024) 136120.
[29] L.Z. Zhang, J.Y. Xu, X.L. Yang, X.Y. Lei, H.H. Sun, Y.H. Huang, H.B. Lu, T.T. Ai, F. Ma b, P.K. Chu, Edge-enriched CeO_2/MoS_2 heterostructure with coupled interface for enabling selective room-temperature NO_2 detection, Sens. Actuators B Chem. 419 (2024) 136443.
[30] B. Das, S. Behera, B. Satpati, R. Ghosh, Layered SnS_2/porous nickel foil based Schottky junction: an excellent ammonia sensor at room temperature, J. Hazard. Mater. 428 (2022) 128252.
[31] Q.X. Zhang, S.Y. Ma, R. Zhang, K.M. Zhu, Y. Tie, S.T. Pei, Optimization NH_3 sensing performance manifested by gas sensor based on Pr-SnS_2/ZnS hierarchical nanoflowers, J. Alloy. Compd. 807 (2019) 151650.
[32] K. Xu, N. Li, D.W. Zeng, S.Q. Tian, S.S. Zhang, D. Hu, C.S. Xie, Interface bonds determined gas-sensing of SnO_2-SnS_2 hybrids to ammonia at room temperature, ACS Appl. Mater. Interfaces 7 (2015) 11359–11368.
[33] Z.Y. Qin, D.W. Zeng, J. Zhang, C.Y. Wu, Y.W. Wen, B. Shan, C.S. Xie, Effect of layer number on recovery rate of WS_2 nanosheets for ammonia detection at room temperature, Appl. Surf. Sci. 414 (2017) 244–250.
[34] S.J. Kim, H.J. Koh, C.E. Ren, O. Kwon, K. Maleski, S.Y. Cho, B. Anasori, C.K. Kim, Y. K. Choi, J. Kim, Y. Gogotsi, H.T. Jung, Metallic $Ti_3C_2T_x$ MXene gas sensors with ultrahigh signal-to-noise ratio, ACS Nano 12 (2018) 986–993.
[35] Z. Yang, L. Jiang, J. Wang, F. Liu, J. He, A. Liu, S. Lv, R. You, X. Yan, P. Sun, C. Wang, Y. Duan, G. Lu, Flexible resistive NO_2 gas sensor of three-dimensional crumpled MXene $Ti_3C_2T_x$/ZnO spheres for room temperature application, Sens. Actuators, B 326 (2021) 128828 (No.).
[36] W. Zheng, Y.S. Xu, L.L. Zheng, C. Yang, N. Pinna, X.H. Liu, J. Zhang, MoS_2 van der waals p–n junctions enabling highly selective room-temperature NO_2 sensor, Adv. Funct. Mater. 30 (2020) 2000435.

Lizhai Zhang received his Ph.D. degree in 2021 from Xi'an Jiaotong University and City University of Hong Kong, China. He is currently working as a Han Jiang Young Scholar of Shaanxi University of Technology. His research interest is the room-temperature gas sensing materials.

Jiayuan Xu received her Master degree in 2021 from Shaanxi University of Technology, China. Her research interest is the first principles calculations.

Xinyu Lei is currently a Master student in Shaanxi University of Technology, China. His research interest is the preparation and sensing application of semiconductor oxides.

Henghui Sun is currently a Master student in Shaanxi University of Technology, China. His research interest is the preparation and sensing application of semiconductor oxides.

Taotao Ai received his Ph.D. degree in 2015 from Shaanxi University of Science and Technology, China. He is currently working as a professor of Shaanxi University of Technology. His research interest is the nanomaterials preparation.

Fei Ma received his Ph.D. degree in 2008 from Xi'an Jiaotong University, China. He is currently working as a professor of Xi'an Jiaotong University. His research interests are the two-dimensional material and chemical sensor.

Paul K Chu received his PhD from Cornell University and is Chair Professor of Materials Engineering at City University of Hong Kong. His research focuses on plasma and materials engineering. He is a fellow of APS, AVS, IEEE, MRS, HKAES, and HKIE and a highly cited researcher.

Edge-enriched SnS_2 nanosheets on graphene for chemiresistive room temperature NH_3 sensors

Lizhai Zhang[a,b,c,e*], *Jiayuan Xu*[d], *Xinyu Lei*[a], *Henghui Sun*[a], *Taotao Ai*[a*], *Fei Ma* [b,e], *Paul K Chu* [c*]

[a] School of Materials Science and Engineering, Shaanxi University of Technology, Hanzhong 723001, Shaanxi, China

[b] State Key Laboratory for Mechanical Behavior of Materials, Xi'an Jiaotong University, Xi'an 710049, Shaanxi, China

[c] Department of Physics, Department of Materials Science and Engineering, and Department of Biomedical Engineering, City University of Hong Kong, Tat Chee Avenue, Kowloon, Hong Kong, China

[d] Natural Active Industrialization Engineering Technology Research Centre of Shaanxi Province, Shaanxi University of Technology, Hanzhong 723001, Shaanxi, China

[e] College of Physics and Information Technology, Shaanxi Normal University, Xi'an 710062, Shaanxi, China

*Address correspondence to: zhanglizhai0512@snut.edu.cn (L. Z. Zhang);

aitaotao0116@126.com (T. T. Ai); paul.chu@cityu.edu.hk (P. K. Chu)

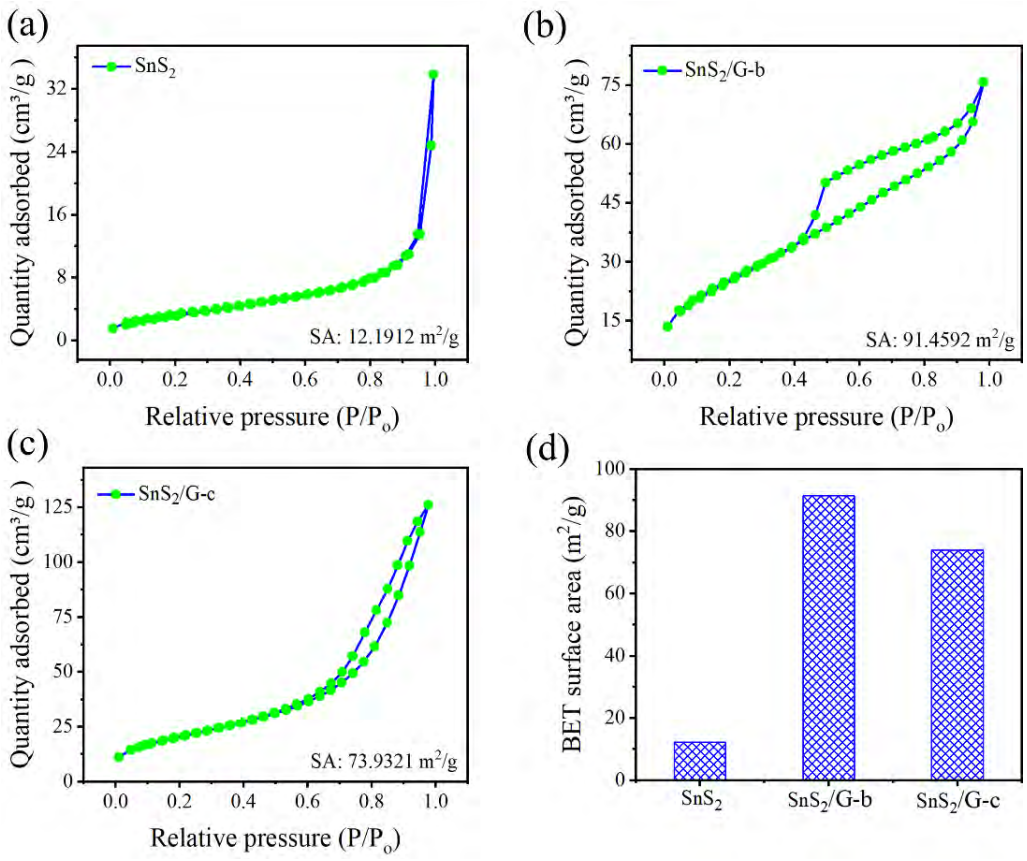

Fig. S1 The Nitrogen adsorption-desorption isotherms of (a) SnS_2, (b) SnS_2/G-b and (c) SnS_2/G-c, (d) BET surface area of SnS_2 and SnS_2/graphene composites.

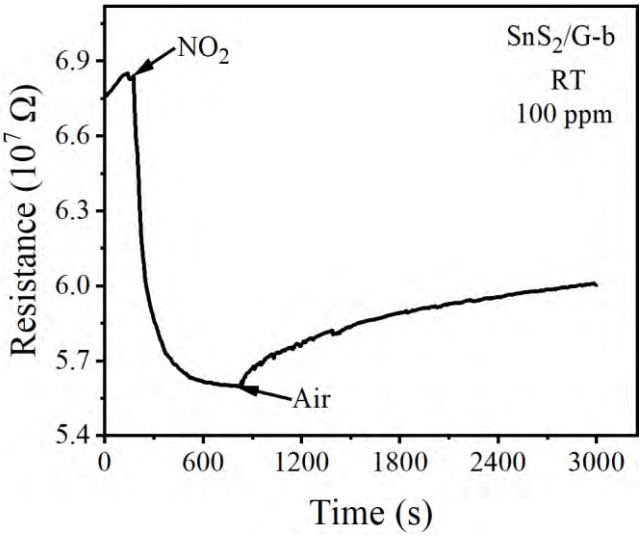

Fig. S2 Real-time resistance variations of SnS_2/G-b to 100 ppm NO_2 at RT

Table S1. Comparison of NH_3 Sensing Properties of sensors in this work with those in the previous work.

Materials	**Working temperature**	**Concentration**	**Response**	**T_{res}/T_{rec} (s)**	**Reference**
SnS_2	200 ℃	100 ppm	86.48%	40.6/624	[8]
SnS_2/ZnS	160 ℃	50 ppm	87.5%	11/22	[31]
SnO_2/SnS_2	RT	100 ppm	47.3%	100/incomplete	[32]
WS_2	RT	250 ppm	2.67%	200/232.3	[33]
SnO_2	RT	100 ppm	No response	No response	[32]
$Ti_3C_2T_x$	RT	100 ppm	0.8%	300/900	[34]
$ZnO/Ti_3C_2T_x$	RT	100 ppm	28.89%	34/103	[35]
SnS_2/graphene	RT	100 ppm	64.38%	63/586	This work